Natural Hazards (2023) 117:491–517
https://doi.org/10.1007/s11069-023-05870-w

ORIGINAL PAPER

Determination of periodic deformation from InSAR results using the FFT time series analysis method in Gediz Graben

K. O. Hastaoglu[1] · F. Poyraz[1] · H. Erdogan[2] · İ. Tiryakioglu[3] · C. Ozkaymak[4] · H. Duman[1] · Y. Gül[5] · S. Guler[1] · A. Dogan[6] · Y. Gul[1]

Received: 5 September 2022 / Accepted: 7 February 2023 / Published online: 21 February 2023

Abstract

Permanent Scatterers (PS) point velocities obtained by the interferometric synthetic aperture radar (InSAR) method are generally determined using the linear regression model, which ignores periodic and seasonal effects. In this study, software was developed that can detect periodic effects by applying fast Fourier transformation (FFT) time series analysis to InSAR results. Using the FFT time series analysis, the periodic components of the surface movements at the PS points were determined, and then the annual velocity values free from periodic effects were obtained. The study area was chosen as the Gediz Graben, a tectonically active region where aseismic surface deformations have been observed in recent years. As a result, using the developed method, seasonal effects were successfully determined with the InSAR method at the PS points in the study area with a period of 384 days and an average amplitude of 19 mm. In addition, groundwater level changes of a water well in the region were modeled, and 0.93 correlation coefficient values were calculated between seasonal InSAR displacement values and water level changes. Thus, using the developed methodology, the relationship between the tectonic movement in the Gediz Graben in Turkey and the seasonal movements and the change in the groundwater level was determined.

Keywords InSAR · Time series analysis · FFT analysis · Seasonal effect

✉ K. O. Hastaoglu
khastaoglu@cumhuriyet.edu.tr

[1] Department of Geomatics Engineering, Sivas Cumhuriyet University, 58140 Sivas, Turkey

[2] Department of Geomatics Engineering, Aksaray University, 68100 Aksaray, Turkey

[3] Department of Geomatics Engineering, Afyon Kocatepe University, 03200 Afyonkarahisar, Turkey

[4] Department of Geological Engineering, Afyon Kocatepe University, 03200 Afyonkarahisar, Turkey

[5] Department of Civil Engineering, Sivas Cumhuriyet University, 58140 Sivas, Turkey

[6] Sarıgöl Vocational School, Manisa Celal Bayar University, 45140 Manisa, Turkey

1 Introduction

Today, Global Navigation Satellite Systems (GNSS) and interferometric synthetic aperture radar methods are generally used for geodetic monitoring of surface movements at cm and below. Considering the cost of GNSS method receivers, measurement cost, and cost of facility and operator for each point, it is an expensive method. In InSAR technology, on the other hand, surface movements can be monitored faster and at lower costs. In addition, the InSAR method can obtain velocities of too many measurement points in large areas. However, the biggest problem here is that the velocities obtained by the multi-temporal InSAR (MT InSAR) method are generally estimated by the regression analysis method, which generally uses the linear model. Ignoring periodic effects on InSAR data leads to misleading results. While these subsidence and uplift are determined by the MT InSAR method, velocities are calculated by generally considering the trend component on the time series. However, the periodic effects in these time series are generally ignored. Therefore, while estimating the velocities of PS points, it is necessary to distinguish the periodic and trend components and then estimate the velocity values free from periodic effects. There are a limited number of studies using different deformation models with different methods in monitoring deformations with the PSInSAR method (Li et al. 2015; Morishita and Hanssen 2015; Wang et al. 2017; Ilieva et al. 2019; Bao et al. 2021; Hu et al. 2021). However, these studies did not use the FFT time series analysis method. Yang et al. (2019), the ratio of the deformations in the dry and rainy seasons to the total deformation was calculated using the Sentinel-1A SAR with the SBAS method, and the seasonal effect was tried to be revealed proportionally. Dalaison and Jolivet (2020), deformations were monitored using the time-dependent Kalman filter method created on the phase differences, and it was determined that the results were compatible with the classical time series analysis results used in the least squares method. Lei et al. (2021), the relationship between the 3D deformations obtained by combining InSAR and GPS technologies and the change in groundwater level was evaluated graphically by observing the trend changes. Khoshlahjeh Azar et al. (2021), SAR deformation and piezometric data were interpolated using a linear model. By calculating the trend of each model, the piezometric relationship with the SAR results was revealed. Zhu et al. (2022), the correlation between surface deformations and groundwater level changes determined by the independent component analysis (ICA) method from Sentinel-1A SAR data of Los Angeles, USA, Santa Ana Basin was determined. For the first time in our study, the FFT analysis method was used to determine the periodic effect on the MT InSAR results, and the success of the method was analyzed. In this study, a post-process FFT-based method has been developed to reveal the seasonal effects and their causes by analyzing the displacement time series obtained from the MT InSAR process.

InSAR is a technique that calculates the phase difference between two different radar images obtained with very close imaging geometries (Massonnet & Feigl 1998; Hanssen 2001; Burgmann et al. 2002; Rosen et al. 2000; Gens & van Genderen 1996). Permanent Scatterers-based PSInSAR is one of the InSAR analysis techniques performed with the help of time series analysis of SAR data taken at different times (Ferretti et al. 2001). The aim is to detect the points (permanent scatterer) showing continuous high reflectivity in each time period from which satellite data is received, monitor them with sub-cm precision, and estimate the relative topographic heights/deformations. Although each PS measurement is given its position relative to a reference point with high precision, the actual measurement uncertainty is low due to uncertainties in the satellite orbit, instrumental problems, delays in the radar signal path, and center uncertainty of the scattering point

(Sousa et al. 2010). Basically, PSInSAR is a powerful method for detecting and monitoring surface deformations (in environments where vertical movement occurs, such as landslides, collapses, and normal faulting.) over time. Each PS can reflect stability problems in buildings, the reflection of changes in groundwater level to the surface (subsidence/ uplift), and deformations caused by the effects of landslides (Cakir et al. 2005). The plane defined by the two angles of incidence of the ascending and descending configurations is called the "co-plane" (Ozawa and Ueda 2011). The LOS changes detected on the interferograms are located in this co-plane. Two components can express the movements detected in the LOS direction in this co-plane. This co-plane is close to being an east–west oriented vertical plane. Therefore, the displacement values are determined with reasonable accuracy for the vertical and eastern components, while for the northern component, they can be determined only to a small extent and are generally unsuccessful. (Fujiwara et al. 2000; Ozawa and Ueda 2011). Monitoring of deformations with the InSAR method is used in different fields, such as monitoring of tectonic movements in the Western Anatolian Menderes region (Arikan et al. 2009), monitoring active volcanoes (Hooper et al. 2004, 2007), earthquake-induced surface movements (Yen et al. 2011; Poyraz et al. 2016), landslides (Peyret et al. 2008; Hastaoglu et al. 2018), monitoring urban areas (Meisina et al. 2006), mine sites (Abdikan et al. 2013; Poyraz et al. 2020), aseismic movements (Poyraz and Hastaoğlu 2020). In recent years, surface deformations obtained from InSAR results have been tried to be associated with external forces that cause these deformations. (Hu et al. 2018; Zheng et al. 2018; Yang et al. 2019; Imamoglu et al. 2019; Shi et al. 2020; Shahzad et al. 2020; Darvishi et al. 2021; Lei et al. 2021; Bui et al. 2021; Khoshlahjeh Azar et al. 2021; Zhu et al. 2022). In many of these studies, the relationship between InSAR surface movements and external force is presented only graphically, and the results are interpreted on these graphs (Zheng et al. 2018; Shi et al. 2020; Shahzad et al. 2020; Lei et al. 2021; Bui et al. 2021). Alternatively, interpretations are made by calculating the correlation values between InSAR surface movements and the external force (Hu et al. 2018; Imamoglu et al. 2019; Darvishi et al. 2021; Zhu et al. 2022; Gezgin 2022). In all these studies, the LOS displacement values obtained using different software are presented graphically, or then the trend is determined by them using the regression method according to the linear model. In all these studies, displacements in the LOS direction were analyzed through a linear regression model, which only includes intercept and trend terms. A linear harmonic regression model, including periodic signals, was not considered. It is well known that trends could be biased when periodic signals are not considered in GPS time series analysis (Blewitt and Lavallée 2002). Even though InSAR and GPS are different techniques, deterministic parameters would be similar if these are indeed not related to hardware. Our study determined the periodic effect using the FFT analysis method.

A geodetic time series such as InSAR time series generically consists of deterministic, e.g., trend, seasonal signals, and stochastic parts. For instance, if an InSAR time series of a selected PS point is analyzed by introducing seasonal signals in addition to the trend parameter, the trend estimates would be unbiased. The consequence of unbiased trend estimates makes interpretations more explicit. Many PSI approaches estimate trend parameters through a linear regression model. The linear model is a necessity to unwrap interferometric phases. However, it might have a drawback on trend estimation if geophysical phenomena are characterized by non-linear deformations (Crosetto et al. 2016). Today, with the evaluation of PSInSAR data, velocity values in the line of sight (LOS) direction of surface movements are calculated by generally determining the trend component, and periodic effects are generally ignored. In this study, the periodic components of the surface movements obtained from the SAR data and the physical causes of these periodic movements

were determined using the FFT time series analysis method. For this purpose, studies have been carried out in the Gediz Graben, which is possible in aseismic seasonal periodic movements and tectonic surface movements in previous studies. Within the scope of the study, tectonic and aseismic movements on the Gediz graben were successfully determined from SAR data by the FFT time series analysis method.

2 Material and methodology

2.1 Study area

This study aims to obtain periodic component and velocity values by subjecting the temporal surface movements of PS points produced as a result of PSInSAR evaluation to time series analysis. For this purpose, Tıraz, Yesilyurt, and Sarigol regions were chosen as the study area (Fig. 1). These areas are located in the eastern part of Gediz Graben in Turkey and are thought to have aseismic deformations apart from the tectonic effect (Koca et al. 2011; Poyraz et al. 2016; Poyraz and Hastaoğlu 2020). Today, the Western Anatolian Expansion Zone (WAEZ) is under the influence of approximately North–South continental expansion at a rate of 30–40 mm/year (Le Pichon et al. 1995; Oral et al. 1995; Bozkurt 2001) and is an area which is effective during Plio-Quaternary. It is typical with NE-SW and EW trending basins that developed under the influence of NS extensional tectonics. The Gediz Graben, in which the study area is located, is one of the most important EW trending neotectonic structures in Western Anatolia (Paton 1992; Seyitoğlu & Scott 1996; Hakyemez et al. 1999; Koçyiğit et al. 1999; Bozkurt & Sözbilir 2004). The graben, which has a northward arcing arc geometry, is approximately 140 km long and 10–15 km wide. According to the active fault map of Turkey updated in 2012 (Emre et al. 2011), the eastern part of the graben, where the study area is located, is represented by three NW–SE trending fault branches between Ahmetli and Sarıgöl. Among the faults mapped in this area, the Alaşehir segment is 45 km long, and the Salihli segment is 30 km long, and they control the southern edge of the graben. The Killik fault, located in the eastern part of the graben,

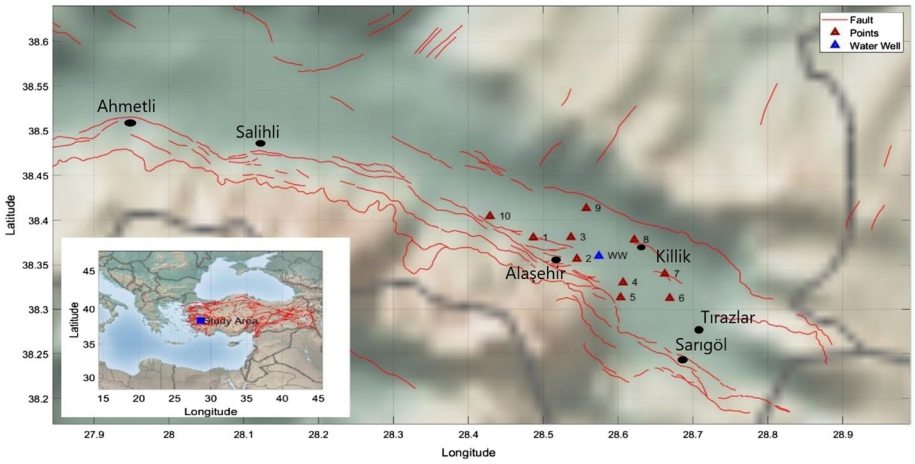

Fig. 1 Study area

is 50 km long and controls the northern edge of the graben. These faults have the potential to produce earthquakes with magnitudes between 6.8 and 7.1 (Duman et al. 2018; Emre et al. 2018). The GPS-based opening velocity in this part of the graben was calculated as 6.4 mm/year (Reilinger et al. 2006; Aktug et al. 2009; Aktuğ et al. 2013). In this section, the southern margin faults of the graben are more active than the northern ones, and morphologically, the southern margin is represented by distinct mountain fronts with a steeper slope. The destructive earthquake (Ms:6.5) that occurred on the Gediz Graben in 1969 and created a surface rupture of approximately 30 km between Sarıgöl in the east and Salihli in the west is the most destructive earthquake known to have occurred in the eastern region of the graben (Arpat & Bingöl 1969; Allen 1974). This earthquake occurred on the Alaşehir segment dipping north from the southern boundary faults of the Gediz Graben.

The velocities obtained by Poyraz et al. (2019) for the GNSS points in the eastern part of the Gediz graben vary horizontally between 12 mm/year and 27 mm/year. When the vertical movements are examined, it is seen that high subsidence values are obtained at the points within the graben. The annual vertical velocity at TRAZ (at Tırazlar locality) was approximately -90 mm/year. BGCL and AKCL points were -33 and -13 mm/year, respectively. It is seen that there are uplifts at the points outside the graben. McClusky et al. (1999), Reilinger et al. (2006), where the velocity area of the Aegean region is calculated as approximately 33 mm/year, and Poyraz et al. (2019) results are similar. In Poyraz et al. (2019), the TRAZ point showed a different movement from the Aegean region's velocity field and the general movement character of the Gediz Graben. It is thought that there are local effects in addition to tectonic effects at and around the TRAZ point. The vertical displacements along the fault were recorded because of areal consolidation settlements (depression), microseismic activity, tectonic cripple, and excessive groundwater withdrawal between 2000 and 2010 in the vicinity of Sarıgöl District (Koca et al. 2011; Demirtaş et al. 2008).

2.2 Data acquisition and evaluation

Sentinel-1A/B images in IW mode used in this study are open-access and obtained from the European Space Agency (ESA). We used 114 radar imageries in descending direction between 2020-05-01 and 2021-12-01 and 116 in ascending direction between 2020–01-04 and 2021–12-06. The temporal resolution of these was 6 days. The track numbers for ascending and descending are 131 and 138, respectively. All of these data were analyzed by adopting the StaMPS PSI method. SeNtinel Application Platform (SNAP) and StaMPS software were used in the analysis. The interferograms were generated through the SNAP software. Here, the master image for both ascending and descending, 2020-12-17 sensed by S1A and 2020-12-12 sensed by S1B (Fig. 2), respectively, was determined through the SNAP. The StaMPS software was used for estimating the LOS velocities.

In the first stage, the steps, splitting the images, correcting the orbits of the satellites, matching the master and slave images, merging, obtaining the interferograms from each pair of images, and topographic phase removal from the interferograms through the SNAP software were performed. Then, the results were exported in a format suitable for the StaMPS software.

In the second stage, StaMPS software, developed by Hooper et al. (2007), was used to obtain the velocities of the PS points in the LOS direction. StaMPS is a software that implements the InSAR permanent scattering method (PS) developed to process in areas subject to deformation in natural or unnatural (buildings, dams, etc.) objects on the earth.

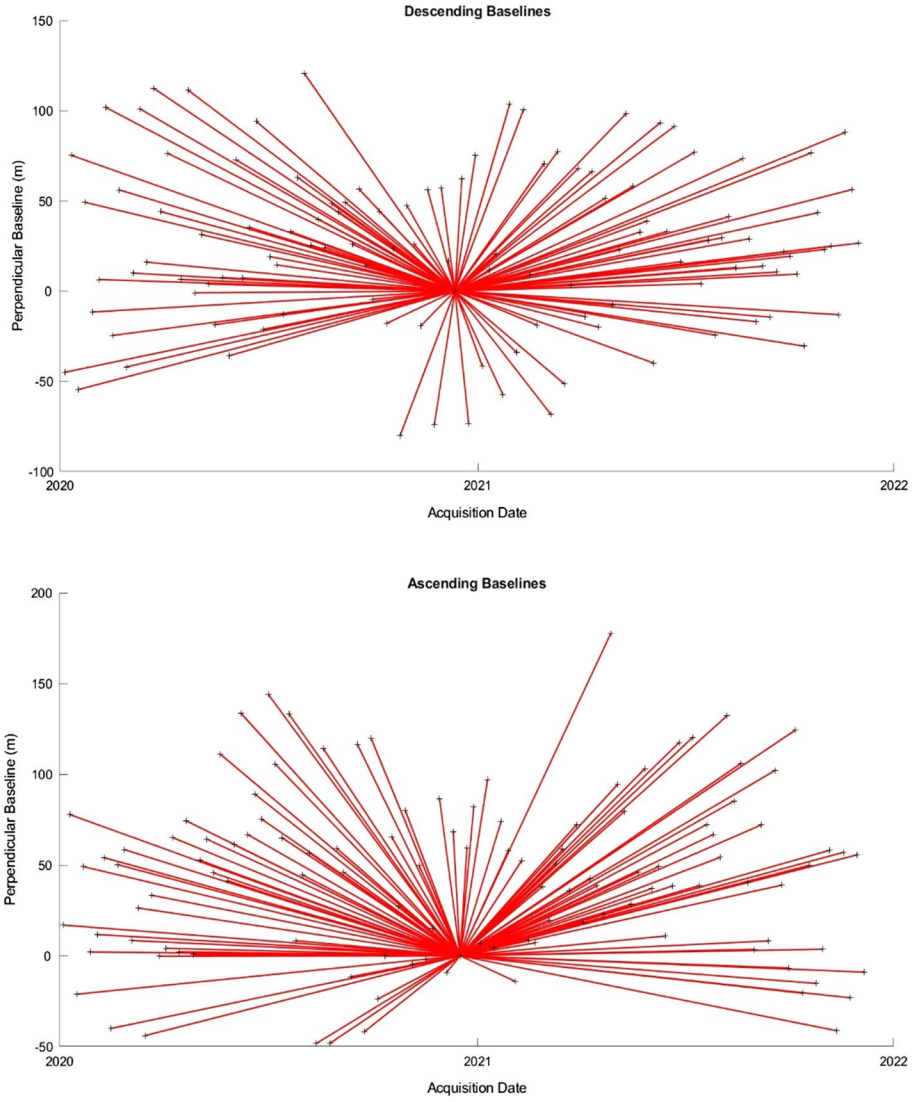

Fig. 2 Baselines

In addition, the pixel amplitude values in each image form the time series. Pixels that are affected by geometric and temporal correlation disorder and have a fixed amplitude value array are selected as PS points. In the PS selection, StaMPS uses amplitude dispersion (DA) to select PS candidates (PSCs). StaMPS filters the PSC phase separately into small patches in spatial and temporal dimensions to divide the correlated interferogram phase into the incidence angle error, deformation trends, and noisy parts. The thresholds for selecting a pixel as PS are determined by calculating the PS probability of each PSC, considering both temporal consistency and amplitude distribution. In the selected PS candidates, the processing approach returned to the wrapped differential interferometric phase

of these PSs and accepted the noise standard deviation of each interferogram as the weighting to calculate the phase due to the spatial uncorrelated look angle error from the wrapped phase (Yao et al. 2020). After that, the deformation series are unwrapped by a three-dimensional unwrapping algorithm (Sousa et al. 2010). In this study, we adopted the amplitude distribution threshold for PS candidates as 0.42 (Sousa et al. 2010). In general, the threshold value range is between 0.40–0.42. Atmospheric correction was introduced using the linear tropospheric correction model of TRAIN software (Bekaert et al. 2015). GACOS data was used for tropospheric delay estimates. (Yu et al. 2018a, 2018b). As a result, a total of 700 days of Sentinel-1A/B data covering the years 2020–2021 were evaluated, and two-year time series were obtained. The LOS velocities obtained as a result of this evaluation are presented in Figs. 3 and 4. LOS velocities values are calculated relative to the mean velocity value in the process area by StaMPS (Serco Italia SPA 2020). Negative values in the LOS direction indicate that the movements move away from the satellite, while positive movements indicate that they approach the satellite. When Figs. 3 and 4 are examined, both descending and ascending satellite data show subsidence in the Graben.

2.3 FFT analysis with the software developed

The behavior of PS point velocities obtained as a result of InSAR evaluations under different effects (linear, periodic, etc.), and size can be explained by the time series analysis. If we denote the displacement of the PS points in the LOS direction with $X(t_i)$, the time series can be written as follows depending on the time.

$$X(t_i) = \underbrace{at_i}_{Trend\ Comp.} + \underbrace{\sum_{s=1}^{r} \left[b_s \cos\left(2\pi f_s t_i\right) + c_s \sin\left(2\pi f_s t_i\right)\right] + v(t_i)}_{Periodic\ Comp.} \quad (1)$$

where a trend component parameters, b_s, c_s periodic component parameters, fs (s = 1,2,….r) frequencies, $v(t_i)$ mean zero, variance σ^2 random are errors. The magnitude of linear or nonlinear change in PS points is significantly affected by periodic movements. Periodic behaviors created by some unmodeled periodic effects at PS points are also determined by time series analysis. In particular, the main source of annual and semiannual periodic changes are external forces such as seasonal weather changes (rain, snow, extreme temperatures, etc.) and groundwater movements. For this reason, the periodic component must be determined by analyzing the time series of PS points. However, frequencies for any significant periodic oscillations must be known to model in Eq. (1). To achieve this, velocities statistically significant should be estimated and removed from the time series. Time series analysis distinguishes the trend, periodic and irregular movements that define the characteristics of the time series system and is frequently applied especially in non-parametric situations. This study aims to determine the periodic movements in the time series by using the FFT method. Therefore, firstly, the trend component in the time series was removed, and then FFT analysis was performed on the remaining series, including periodic and irregular movements. For the separation of the trend component from the series, it is obtained with the least squares method and a time-dependent equation ($Y_t = a + b.t$). The coefficients of the obtained equation are calculated by regression analysis. According to the least squares method, with a and b unknown parameters, and standard deviations of the parameter (s_a, s_b) are calculated. To test whether the calculated parameters are significant, the test value (parameter /standard deviation of the parameter) was compared with the student(t)-distribution value for 95% level of confidence. Otherwise, the

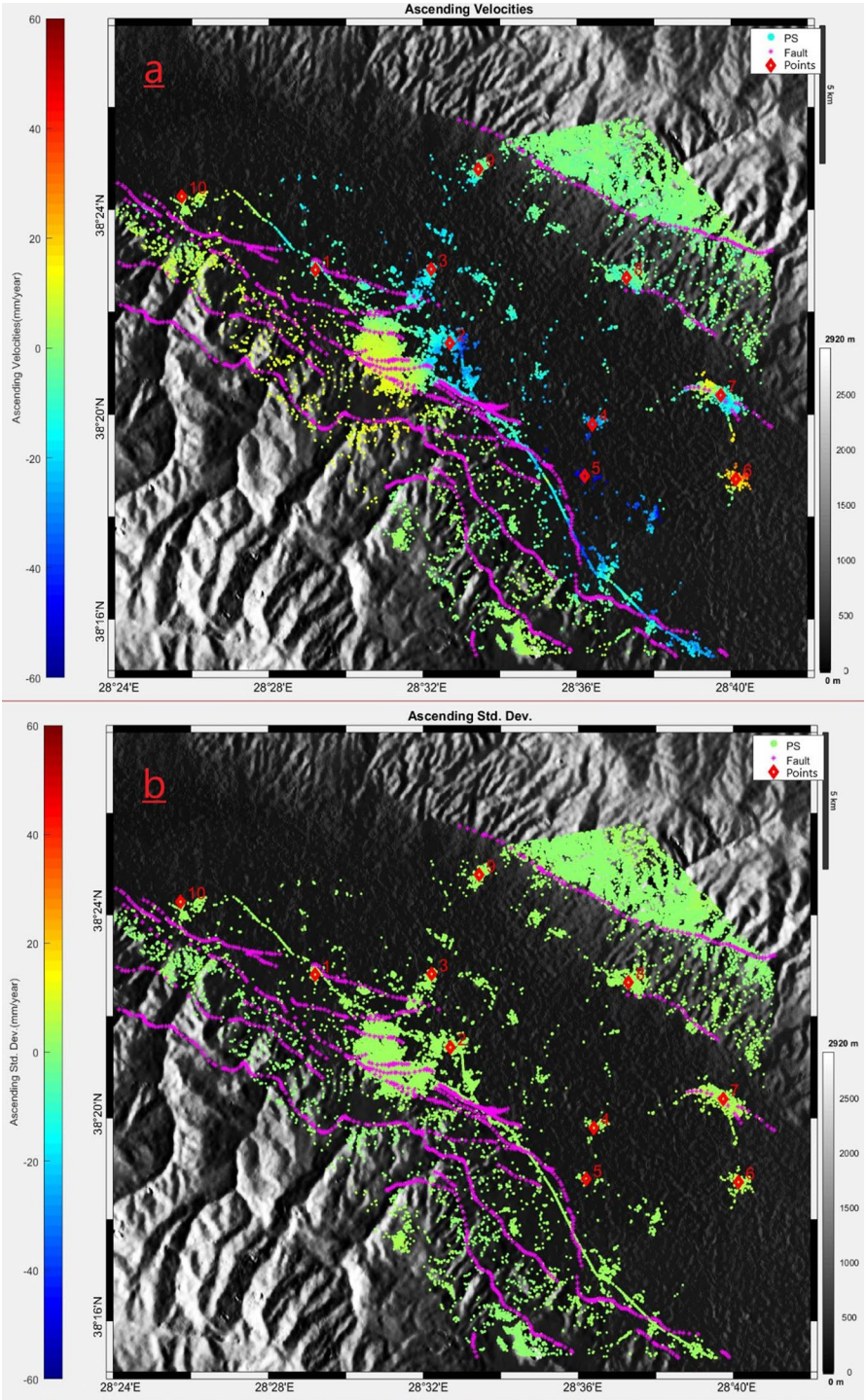

Fig. 3 **a** Velocity values in the LOS direction of the ascending orbit with trace number 131 (January2020-January2022), **b** Standard deviation values of the ascending orbit with trace number 131

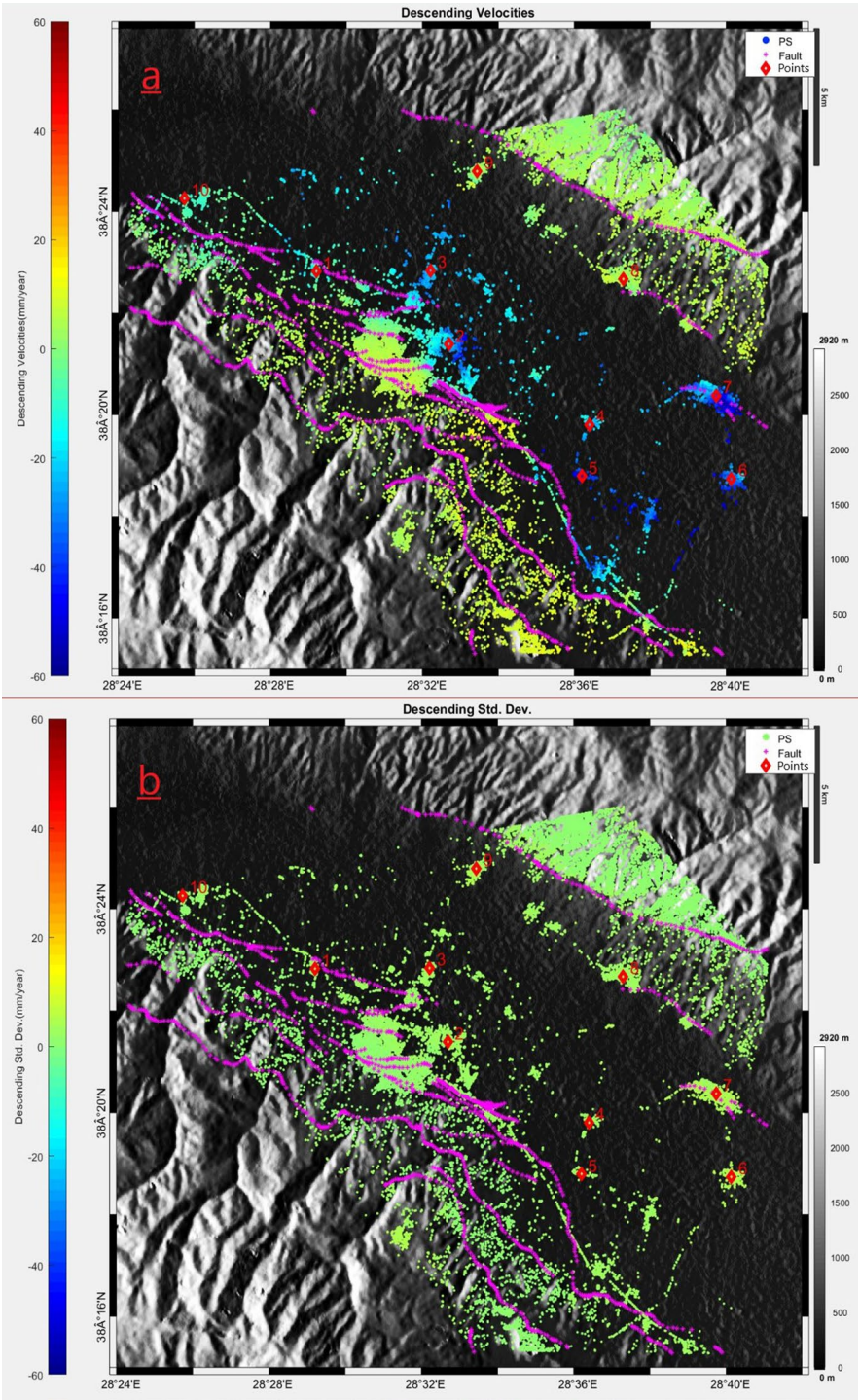

Fig. 4 **a** Velocity values in the LOS direction of the descending orbit with trace number 138 (January2020-January2022), **a**, **b** Standard deviation values of the descending orbit with trace number 138

linear trend component in the series affects the spectral analysis results and gives a peak at zero frequency. For the separation of the trend component from the series, it is obtained with the least squares method and a time-dependent equation ($Y_t = a + b.t$). The coefficients of the obtained equation are calculated by regression analysis.

The trend component removed series from the time domain to the frequency domain is transformed with the fast Fourier transform (FFT) given by Eq. 2. FFT is a highly optimized implementation of the discrete Fourier transform (DFT), which converts discrete signals from the time domain to the frequency domain. FFT computations provide information about the signal's frequency content, phase, and other properties (Frigo & Johnson 1998).

$$X(f) = \sum_{t_i=0}^{N-1} P(t_i) \cdot e^{-if\frac{2\pi}{N}t_i} \tag{2}$$

In Eq. 2, the value of X(f) and $e^{2\pi jt}$ represent the complex and exponential function. Since the values obtained from the FFT are complex numbers, they are still insufficient to determine the series' frequencies. Therefore, the square of the modulus of X(f) is calculated, and so called as Fourier spectrum $P_{xx}(f)$.

$$P_{xx}(f) = |X(f)|^2 \tag{3}$$

Thus, by detecting at which frequencies the energy of a signal is concentrated, the frequencies of the periodic movements existing in the series are determined. These frequencies are replaced in the periodic component in Eq. (1), and the frequency parameters bs, cs are tested (Fig. 6). Insignificant parameter frequencies are removed from the function, and this process is continued until significant parameter frequencies are only left. At last, the parameters of the time series are composed of trend and periodic signals statistically significant through FFT in Eq. (1). Additionally, the amplitude values of the periodic signals are determined.

In light of the method described above, software was developed that automatically performs FFT time series analysis of PS data using the MATLAB programming language. The software algorithm is presented in Fig. 5. The developed software computes the discrete Fourier transform (DFT) using an FFT algorithm. FFT analysis is generally applied to equally spaced data. Since the Sentinel 1A/B data are published in equally 6-day periods, it is thought that the FFT method will be successfully applied to the equally 6-day displacement data produced from the Sentinel 1A/B data. Sometimes, interruptions occur in Sentinel 1A/B data due to hardware problems. The DFT method works successfully in the analysis of time series with such temporal discontinuities. Munteanu et al. (2016) stated that FFT produces better results than other tested methods for reliably estimating the spectral slope of a signal recorded in a turbulent environment when the time series data contains gaps. Considering that the gaps in the InSAR results will not cover large time intervals, it was thought that there would be no problem in using the DFT method in the InSAR time series analysis.

3 Analysis and results

In the LOS velocity, values obtained from the descending and ascending satellite data, 10 points that will provide the general distribution on the graben, especially where the settlement areas are located, were determined, and FFT time series analyzes were performed at these points. Thus, the characteristics of the movement at these points were

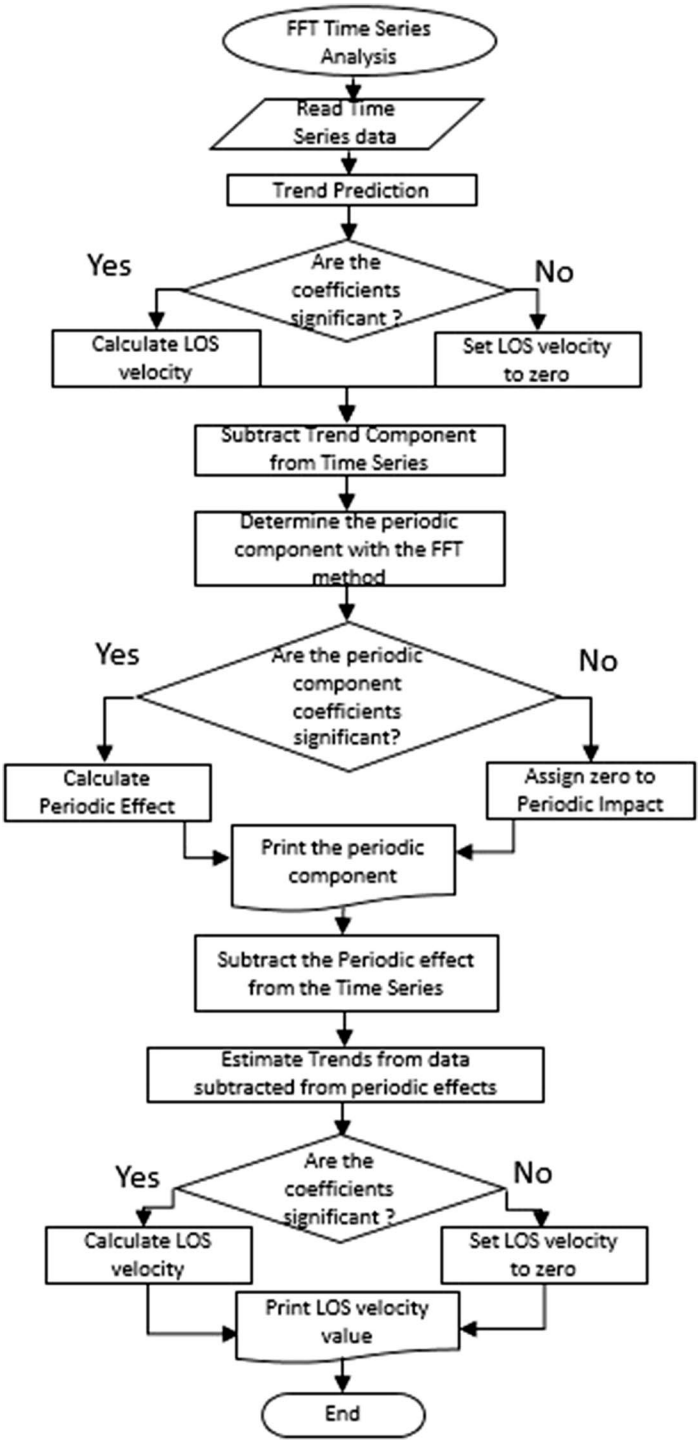

Fig. 5 Software FFT process flow chart

Fig. 6 **a** Selected points for FFT analysis, ILGIN water well and faults on horizontal velocities obtained from decomposing ascending and descending satellite radar images, **b** Selected points for FFT analysis, ILGIN water well and faults on vertical velocities obtained from decomposing ascending and descending satellite radar images

examined. Figure 6 shows the locations of the selected points on the ascending satellite LOS velocities and the underground water level monitoring well in the region.

For the selected points, using the software developed within the scope of the study, FFT time series analyzes were performed on the ascending and descending satellite data, respectively. Figures 7 and 8 present graphs of the software output FFT analysis results obtained from the ascending and descending satellite data of the fifth point with the highest deformation.

FFT analysis results for PS point 5 are presented in Figs. 7 and 8. The graph, expressed as "Point id 5 Time Series" in Figs. 7 and 8, shows the 700-day displacement values for point 5 descending and ascending satellites. In the graph expressed by "Point id 5 Trend Estimation", the trend component (for $m=2$ in Eq. 1) and velocity values calculated according to the $Y=a_1+a_2*t$ linear function with least squares method (LSM) from displacement data are presented. The a_1 and a_2 parameters and standard deviations of the linear function were calculated according to LSM, and the significance of the calculated parameters was tested according to the t-distribution for the degree of freedom ($f_1=114$ and $f_2=112$) and 95% ($\alpha=0.05$) confidence level. These results are presented under the title of "Trend Estimation" of the report presented in Figs. 7 and 8. The important thing here is whether the a2 parameter depending on t (time: taken as days) is significant or not. Because the parameter that will be used to determine the change, that is, the magnitude and the direction of the velocity, is a2. The annual velocity value at a point is calculated as velocity $=a_2*365$.

Figures 7 and 8 show the spectrum values for the frequencies obtained as a result of the FFT analysis in the "Point id 5 Fourier Spectrum" graph. For example, here the frequency value with the maximum spectrum value is determined as 0.00260. Thus, the period duration was determined as $1/0.00260=384$ days. The trigonometric functions of the determined frequencies, that is, the harmonic parameters and the standard deviations of these parameters are determined according to the LSM. Then, these parameters are tested to determine whether they are significant, similar to testing the parameters in a linear function. These results are presented in Figs. 7 and 8 under the report section "Estimation of Periodic Effect". In Figs. 7 and 8, "Point id 5 Trend Free Data" graph, the graph of the displacement data free from the trend component and the periodic component determined as a result of the FFT analysis are presented. In the graph presented under the title of "Point id 5 Trend + Periodic Effect" in Figs. 7 and 8, the curve of the model, which includes liner and periodic movements estimated according to displacement values, is presented. Under the title of "Point id 5 Periodic Effect Free Data", displacement values free from periodic effect are presented. Then, new trend component and velocity values are calculated from the displacement values free from periodic effects, and these values are presented in the "Point id 5 Trend Estimation from Periodic Effect Free" graphic and under the "Trend Estimation from Periodic Effect-free Data" heading of the report in Fig. 7 and 8. Thus, using FFT analysis for PS point 5, new velocity values free from periodic effects were calculated. Finally, the estimated new trend and periodic model for the data are presented in the "Point id 5 New Trend + Periodic Effect" graph.

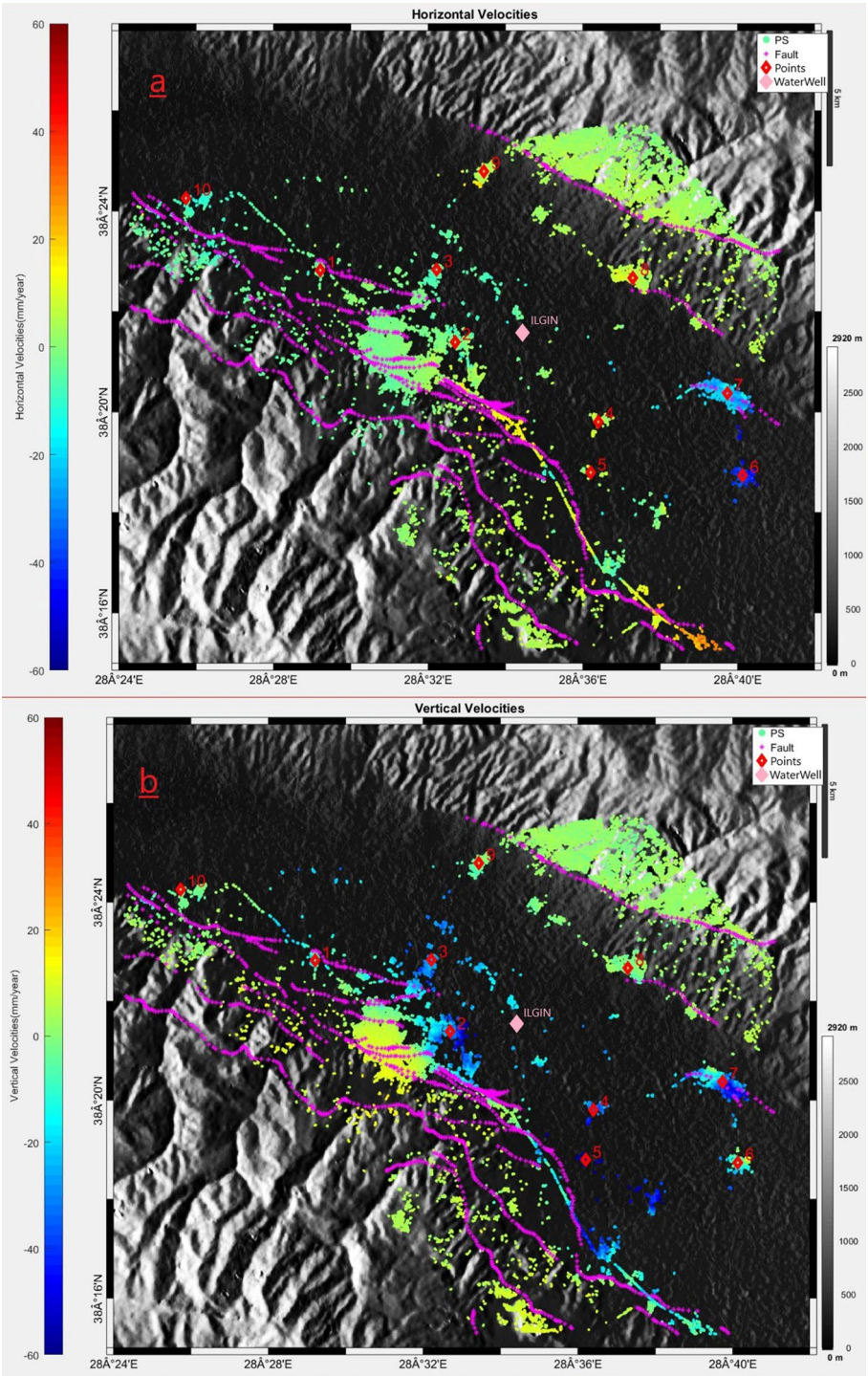
Horizontal Velocities
a
PS
Fault
Points
WaterWell
5 km
ILGIN
Horizontal Velocities(mm/year)
60
40
20
0
-20
-40
-60
38Â°24'N
38Â°20'N
38Â°16'N
28Â°24'E
28Â°28'E
28Â°32'E
28Â°36'E
28Â°40'E
2920 m
2500
2000
1500
1000
500
0
0 m
Vertical Velocities
b
PS
Fault
Points
WaterWell
5 km
ILGIN
Vertical Velocities(mm/year)
60
40
20
0
-20
-40
-60
38Â°24'N
38Â°20'N
38Â°16'N
28Â°24'E
28Â°28'E
28Â°32'E
28Â°36'E
28Â°40'E
2920 m
2500
2000
1500
1000
500
0
0 m

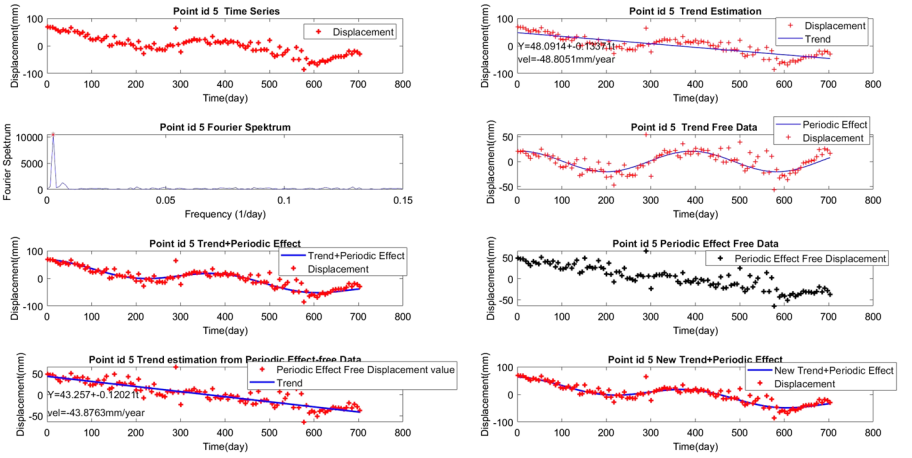


```
 Point id 5  Time Series Analysis

Trend Estimation
========        ======  =====   =====   ===========
Coefficient     mx(mm)  TestV.  t-dist.  Decision
========        ======  =====   =====   ===========
 -0.134         0.009           14.32           1.66            significant
 Annual Velocity Value = -48.805 mm/year

************************************************************

 Estimation of Periodic Effect
Amplitude(mm)   Frequency(1/day)        Period (day)    Coefficient             mx(mm)  TestV.          t-dist.          Decision
======  ========        ========        ========        ======  =====   =====   ===========
 20.523         0.00260         384.00          2.383                   1.75            1.36            1.66            unsignificant
 20.523         0.00260         384.00          20.384                  1.83            11.16           1.66            significant
*************************************************************************************************************

Trend estimation from Periodic Effect-free Data
========        ======  =====   =====   ===========
Coefficient     mx(mm)  TestV.  t-dist.  Decision
========        ======  =====   =====   ===========
 -0.120         0.009           25.52           1.66            significant
 Annual Velocity Value = -43.876 mm/year
```

Fig. 7 FFT analysis graphs and report of point 5 from LOS velocities obtained from ascending satellite images with trace number 131

Periodic effects are clearly observed for both ascending and descending satellite data in Figs. 7 and 8. In both data, effects are observed in a period of approximately one year. When Fig. 7 is examined, a cosinesoidal effect with an amplitude of 20.5 mm and a period of 384 days was determined at point 5 for the ascending satellite. When this periodic effect is removed from the data set, the annual velocity value decreases from approximately -49 mm to -44 mm. When Fig. 8 is examined, a cosinesoidal effect with an amplitude of 18.8 mm and a period of 384 days was determined at point 5 for the descending satellite. When this periodic effect is removed from the data set, the annual velocity value decreases from approximately -53 mm to -49 mm. There is a 10% change in the velocity value due to the periodic effect in both satellite data. FFT analysis was performed in all other 10 points. FFT analysis results for all points are presented in Table 1.

Periodic effects with amplitudes ranging from 14 to 25 mm and a period of 384 days were modeled at all points. An average of 23.5% change was observed for the ascending satellites, and 8.5% for the descending satellites in the velocity values estimated from the displacement values cleaned from periodic effect. Periodic effects with an average amplitude of 19 mm were observed for descending and ascending satellites. In the results of the FFT analysis, a movement pattern with a nearly one-year period, which is stable in winter, subsidence in spring and summer, and slightly uplift in autumn, has been determined.

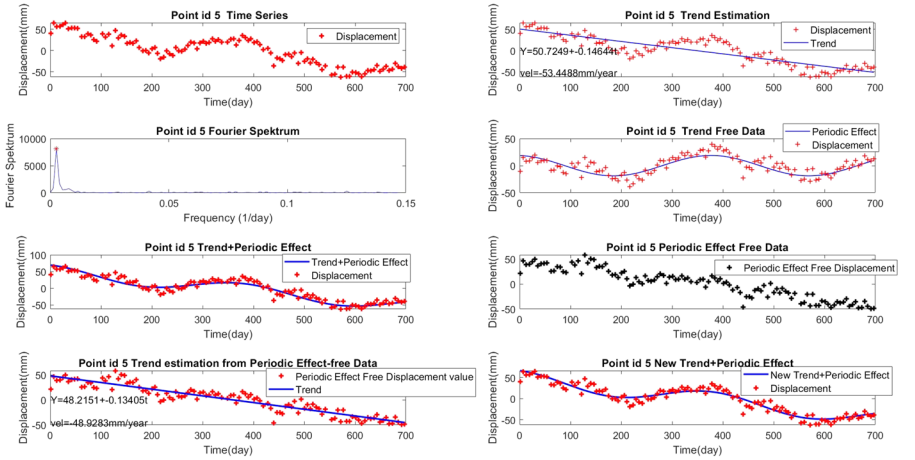


```
 Point id 5  Time Series Analysis

Trend Estimation
========        ======  =====   =====   ===========
Coefficient     mx(mm)  TestV.  t-dist.  Decision
========        ======  =====   =====   ===========
 -0.146         0.008           17.56           1.66            significant
 Annual Velocity Value = -53.449 mm/year

************************************************************

 Estimation of Periodic Effect
Amplitude(mm)   Frequency(1/day)       Period (day)    Coefficient             mx(mm)  TestV.          t-dist.          Decision
======  ========        ========        ========        ======  =====   =====   ===========
 18.831         0.00260         384.00          -2.251                  1.42            1.58            1.66            unsignificant
 18.831         0.00260         384.00          18.696                  1.46            12.77           1.66            significant
************************************************************************************************************

Trend estimation from Periodic Effect-free Data
========        ======  =====   =====   ===========
Coefficient     mx(mm)  TestV.  t-dist.  Decision
========        ======  =====   =====   ===========
 -0.134         0.008           27.65           1.66            significant
 Annual Velocity Value = -48.928 mm/year
```

Fig. 8 FFT analysis graphs and report of point 5 from LOS velocities obtained from descending satellite images with trace number 138

The data of descending and ascending satellites were converted into up and east components from the LOS direction by using the formulas presented in Eq. 4 (Hanssen 2001).

$$\begin{pmatrix} -\cos\left(\alpha_{ASC}\right) & \sin\left(\alpha_{ASC}\right)X\cos\left(\delta_{ASC}\right) \\ -\cos\left(\alpha_{DSC}\right) & \sin\left(\alpha_{DSC}\right)X\cos\left(\delta_{DSC}\right) \end{pmatrix}\begin{pmatrix} V_{UP} \\ V_{EW} \end{pmatrix} = \begin{pmatrix} V_{LOS,ASC} \\ V_{LOS,DSC} \end{pmatrix} \tag{4}$$

In Eq. 4, for ascending and descending satellites,α_{ASC}, α_{DSC} show the heading angles, andδ_{ASC}, δ_{DSC} show the incidence angles.V_{UP}: velocity for the up component, V_{EW}: velocity for the east component, $V_{LOS,ASC}$: velocity in the LOS direction of the ascending satellite, $V_{LOS,DES}$: velocity in the LOS direction of the descending satellite. The surface movements in the North–South direction can only be determined between 10–15% of the actual deformation amount with the SAR method due to the North–South orientation of the SAR satellites' orbits and the side-looking radars of the SAR satellites. Therefore, in many SAR studies, the deformations in the north direction are assumed to be zero, and the two-dimensional transformation matrix in Eq. 4 is used (Pawluszek-Filipiak and Borkowski 2020). As can be seen in the equation in Eq. 4, since two ascending and descending LOS values of a pixel are measured, only the unknown in two directions can be solved. In addition, using Sentinel1A and Sentinel 1B descending and ascending LOS values of the same pixel, four equations can be obtained, and the unknowns in three directions can be solved. However, in this case, the matrix performance deteriorates due to the very small coefficient values in

Table 1 LOS direction FFT analysis results for all points

Point ID	Ascending				Descending			
	Vel.[a] (mm/y)	Period (day)	Ampl. (mm)	Vel.[b] (mm/y)	Vel.[a] (mm/y)	Period (day)	Ampl. (mm)	Vel.[b] (mm/y)
1	− 6.65	384	16.63	− 5.19	− 13.21	384	14.19	− 11.55
2	− 20.56	384	23.09	− 14.35	− 23.02	384	18.20	− 20.21
3	− 11.72	384	16.59	− 6.80	− 25.66	384	19.03	− 23.18
4	− 32.47	384	20.98	− 28.29	− 26.87	384	20.26	− 23.59
5	− 48.80	384	20.52	− 43.87	− 53.45	384	18.83	− 48.93
6	22.57	384	20.93	19.34	− 36.03	384	22.78	− 35.55
7	− 14.85	384	16.03	− 15.64	− 40.00	384	16.09	− 43.09
8	− 7.75	384	22.37	− 4.91	0.00	384	22.93	0.00
9	− 7.34	384	19.07	− 4.56	0.00	384	24.63	0.00
10	0.00	384	14.77	5.41	− 10.95	384	15.33	− 10.55

[a]The velocity estimates considering periodic effect

[b]The velocity estimates not considering periodic effect

the North–South direction, and realistic results cannot be obtained. The condition number of a matrix (cond) is a measure of the sensitivity of the solution of a system of linear equations to errors in the data. It indicates the accuracy of the results from matrix inversion and linear equation solutions. For a correct solution, this value should not exceed 1. However, this value is around 10 in the A coefficients matrix used for the transformation from LOS to three dimensions with the least square estimation method, causing the results to be erroneous (Fuhrmann & Garthwaite 2019). Therefore, unfortunately, only the two-dimensional transformation in Eq. 4 can be performed using existing satellite configurations. Using the developed software, the displacement values in the up and east directions were calculated using the displacement values in the descending and ascending LOS directions of 10 points in the study area. Then, trend and periodic components were determined by performing FFT analysis for the up and east directions. Figure 9 presents the FFT analysis outputs for the up and east components of point 5. When Fig. 9 is examined, the velocity value for the up component changed from -70 mm/year before the analysis to -62 mm/year after the analysis, and the seasonal effect was determined in a 384-day period. For the east component, the velocity value was determined as 0 mm/year. In Table 2, the results of the up and east components FFT analysis for all 10 points are presented.

When Table 2 is examined, in accordance with the general deformation character of the Gediz Graben, subsidence with velocities of approximately 10 to 60 mm/year were detected at points 1–7 falling into the graben, while values close to zero were obtained at points 8, 9, and 10, which are partially on the graben boundary. In addition, small movements in the small EW direction were detected. Especially at points 6 and 7, besides vertical movement, significant horizontal movements were determined. Especially at point 6, a westward movement was determined at a velocity of approximately 43 mm/year. A periodic effect with an amplitude varying between 19–30 mm in a period of 384 days was determined at all points in the vertical direction. In addition to this, 384-day periodic effects with amplitudes varying between 3–7 mm were determined, except for points 6 and 7 in the horizontal direction. At points 6 and 7, different from the general movement, 256-day periodic effects were determined. Already at points 6 and 7, unlike other points, dominant movements were observed in the west direction. At points 6 and 7, movements seem to be different from the graben behavior. By examining these and their neighboring points visually, it is suspected there could be a possible buried normal fault. Any outcrops were not observed in the field study not because an alluvial formation covers the graben but because physical conditions of surface cover is changing wherefore intensive agricultural activities.

As can be seen from Table 2, the general dominant movement character of the graben is subsidence, and a periodic effect of 384 days has been determined for the up component of all points. In order to examine the reasons for this periodic effect, the underground level change values of the Ilgın water well in the region between 2013 and 2018 were obtained from İzmir Regional Directorate for State Hydraulic Works (DSI in Turkish). Since DSI could not measure water wells during the COVID-19 pandemic, groundwater levels are available until 2018. Then, these values were subjected to FFT and periodic component analysis in order to determine the groundwater level change model. Although it is known that the amplitude of the periodic effect decreases as a result of applying the FFT analysis to the data with large gaps, the FFT analysis method was used because the main purpose here is to reveal the general characteristics of the groundwater level change. In Fig. 10, monthly groundwater level changes and FFT and periodic component analysis results of the ILGIN water well in the Graben are given between January 2013 and November 2018.

As a result of the analysis of the groundwater level values of the Ilgın water well, a model with an amplitude of 4.16 m and a period of 393 days was determined. This periodic

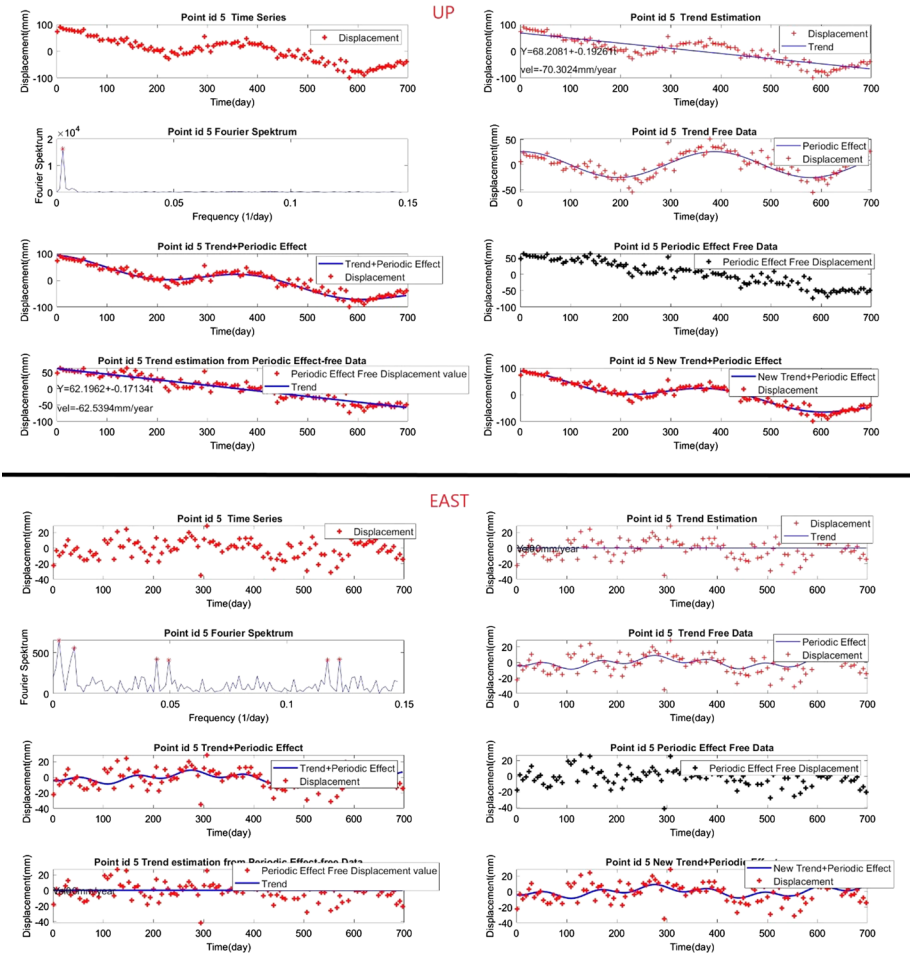

Fig. 9 After decomposing, Up and East FFT analysis outputs of point 5

groundwater level change and the 384-day periodic displacement movement obtained from the PS results are in harmony. This suggests that the main reason for the seasonal effects in the region is the change in groundwater level. Therefore, the relationship between groundwater level and InSAR displacement values has been studied in more detail.

Figure 11 shows the average monthly precipitation amounts between 1962 and 1995 at Alaşehir District Meteorology Observation Station (Dikmen et al. 2019), and the average monthly water levels of the Ilgın water well between 2013 and 2018 are presented. A correlation coefficient of 0.78 was calculated between groundwater levels and precipitation amounts. As it can be understood from here, the main source of groundwater in the region is seasonal precipitation.

In Fig. 12, vertical displacement and groundwater level models obtained as a result of FFT analysis are presented. As stated in Eser Mühendislik Müsavirlik (2014), the groundwater recharge is 142×106 m^3/year in the Salihli-Alaşehir-Sarıgöl region, which also

Table 2 Up and east component FFT analysis results for all points

Point ID	UP				East			
	Vel.[a] (mm/y)	Period (day)	Ampl. (mm)	Vel.[b] (mm/y)	Vel.[a] (mm/y)	Period (day)	Ampl. (mm)	Vel.[b] (mm/y)
1	− 14.07	384	20.58	− 10.82	− 3.30	384	3.3	− 4.93
2	− 30.62	384	26.80	− 23.79	0.00	384	7.27	− 4.03
3	− 26.07	384	23.01	− 20.524	− 9.15	384	7.67	− 11.82
4	− 41.21	384	26.67	− 35.48	6.93	384	7.34	0.00
5	− 70.30	384	25.88	− 62.54	0.00	384	5.03	0.00
6	− 12.04	384	29.50	− 14.37	− 42.66	256, 109	6.32, 5.50	− 43.57
7	− 41.05	384	21.38	− 43.07	− 18.11	256	9.00	− 19.15
8	0.00	384	30.13	0.00	7.66	384	6.17	4.16
9	− 7.87	384	27.56	− 4.15	4.62	384,128	6.11, 2.56	2.60
10	− 5.46	384	19.27	− 3.12	− 10.95	384,128	4.28, 1.27	− 12.52

[a]The velocity estimates considering periodic effect

[b]The velocity estimates not considering periodic effect

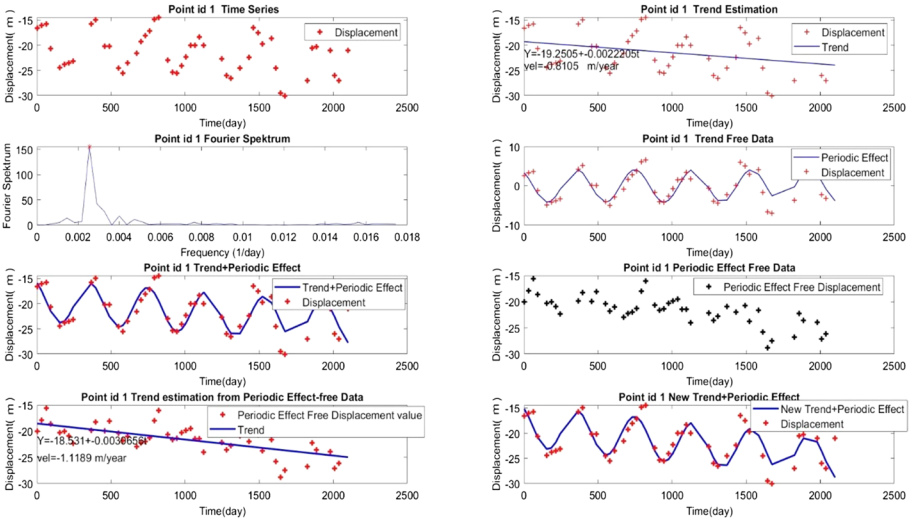


```
01-Mar-2022 00:13:53
Time Series Analysis
----------------------------------------
Number of Point Number of Mesurment     Confidence Level        Degrees of Freedom
=============   ==================      ==================      ==================
   1                49                      %95                     47
*****************************************************************************************************

 Point id ILGIN  Time Series Analysis

==========  ======  =====   ======   ==========
Coefficient  mx( m)  TestV.  t-dist.  Decision
==========  ======  =====   ======   ==========
 -0.002      0.001   2.35    1.68     significant
 Annual Velocity Value = -0.810 m/year

*****************************************************************************************************

 Estimation of Periodic Effect
=============   ================  ============  ===========  ======  =====   ======   =============
Amplitude( m)   Frequency(1/day)  Period (day)  Coefficient  mx( m)  TestV.  t-dist.  Decision
=============   ================  ============  ===========  ======  =====   ======   =============
  4.161         0.00254           393.14        -2.371       0.47    5.07    1.68     significant
  4.161         0.00254           393.14        3.420        0.49    6.93    1.68     significant
*****************************************************************************************************

Trend estimation from Periodic Effect-free Data
==========  ======  =====   ======   ==========
Coefficient  mx( m)  TestV.  t-dist.  Decision
==========  ======  =====   ======   ==========
 -0.003      0.001   5.93    1.68     significant
 Annual Velocity Value = -1.119 m/year

-----------------------------------------------------------------------------------------------------
```

Fig. 10 ILGIN water well groundwater level changes

includes the study area, while the draft and discharge are 165×106 m^3/year. In summary, groundwater reserve change in the region is 23×106 m^3/year. As it can be understood from here, unplanned and excessive underground water withdrawal and discharge take place in the region. When Fig. 12 is examined, a decrease is observed in the groundwater level between January and August. The main reason for this decrease is the decreasing amount of precipitation in the region since January (Fig. 11) and the agricultural activities that started in March. Groundwater is mostly used in agricultural activities in the region. Depending on both the increase in the use of groundwater for agricultural purposes and the decrease in precipitation amounts, decreases in water levels are observed in the spring and summer months. In the autumn, there is an increase in groundwater levels again due to the increasing rainfall in the region and the decrease in agricultural irrigation. In general, the groundwater level in the region has a decreasing trend, and the decrease accelerates in the spring and summer months, and the water level rises in the autumn. When the vertical displacement motion patterns in the region, presented in Fig. 12, are examined in detail, a

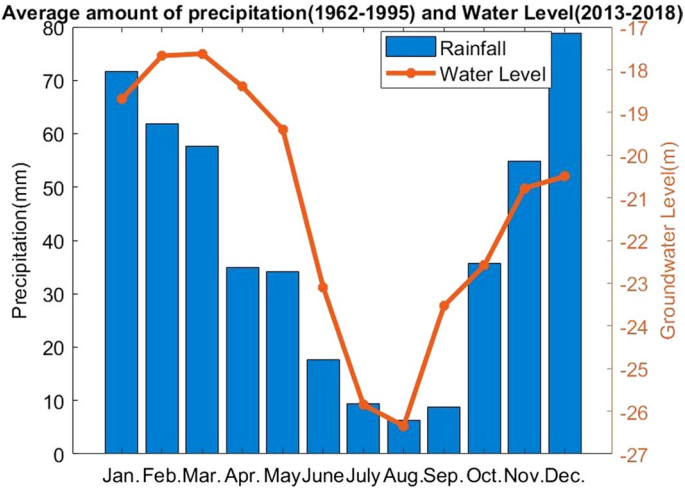

Fig. 11 Average amount of precipitation (1962–1995) and water level (2013–2018)

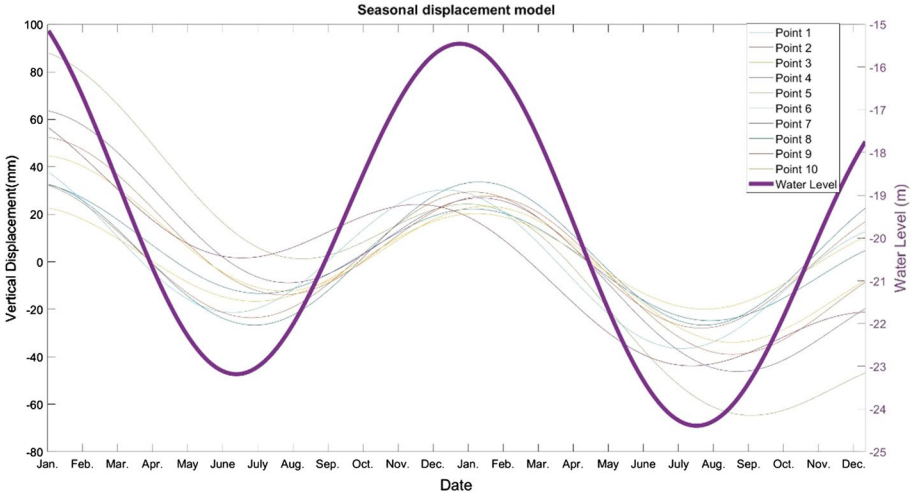

Fig. 12 InSAR vertical displacement model and groundwater level models determined by FFT analysis

subsidence trend is observed at all points depending on the general tectonic structure of the graben. However, in addition to this trend, especially between August and December, the rate of subsidence approaches zero and even tends to uplift. In summary, while the general subsidence trend increases in January-August, this movement slows down between August and January and even shows a slight uplift trend. This movement pattern clearly shows the existence of the seasonal effect. It is clearly observed from Fig. 12 that the groundwater level change is the main reason for this seasonal effect. In order to reveal this relationship more clearly, seasonal groundwater level change values were calculated from the periodic component model, which is free from the trend component for the groundwater

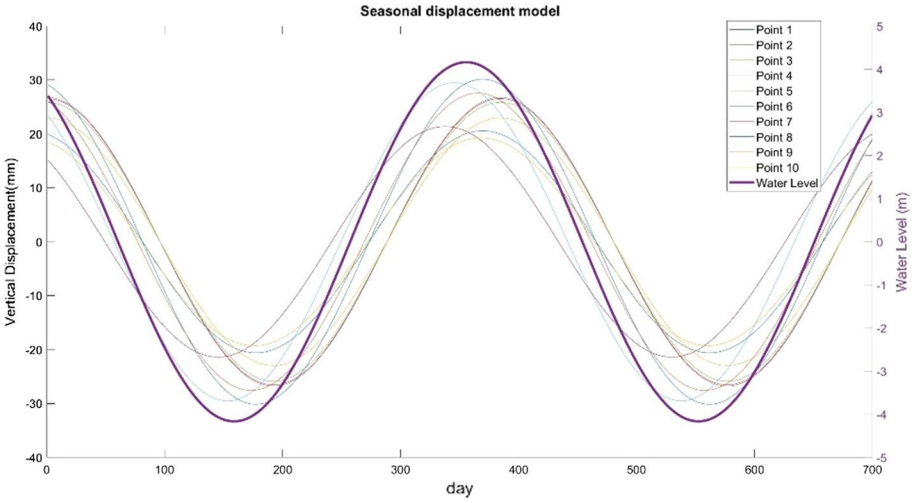

Fig. 13 Groundwater level and vertical displacement seasonal movement patterns

Table 3 Correlation coefficient (R) values between the underground level seasonal motion model value and the seasonal vertical displacement model values of the points

P.ID	1	2	3	4	5	6	7	8	9	10
R	0.97	0.877	0.877	0.877	0.877	0.97	0.94	0.96	0.98	0.97

level values. Likewise, seasonal vertical displacement values at the points were calculated according to the trend-free periodic component model (Fig. 13). Then, the correlation coefficient values between the seasonal changes in the groundwater level and the seasonal displacement values at the points were calculated (Table 3).

When Table 3 and Fig. 13 are examined, it is observed that there is a very high correlation between the seasonal behavior of the groundwater level and the seasonal behavior of vertical displacement values. The effect of groundwater level on vertical displacement values is clearly observed in Table 3 and Fig. 13. While the rate of subsidence in the graben increases during the periods when the groundwater level decreases in January-August, the rate of subsidence slows down and even shows a slight uplift trend during the periods when the groundwater level increases in August-January. As a result, the seasonal surface deformation model in the Gediz graben and the relationship of these seasonal movements with the groundwater level have been successfully determined.

4 Conclusions

According to the data obtained, vertical displacements (subsidence) with a velocity of approximately 10 to 62 mm/year have been detected at the base of the graben (at points 1–7) within a two-year period (between 2020 and 2022). Considering that the long-term average vertical slip rates calculated on some normal faults in Western Anatolia vary

between 0.1 and 0.5 mm/year (Özkaymak et al. 2011, 2015, 2019; Kürçer et al. 2021). It is clear that these values obtained along the Alaşehir segment are largely not of tectonic origin. However, it can be said that the areas where subsidence is detected are bordered by faults, and lithology control is also effective. For instance, the points (e.g., 8 and 9) located in the northern part of the graben depict 0–4 mm/year LOS velocities. This part geologically accompanies the normal faults showing minimum activity and unconsolidated alluvial lithology. Additionally, the area (e.g., the points 2, 3, 4, 5, and 7), bounded by Alaşehir in the west, Bağlıca in the east, Delemenler in the south, and Killik in the North, reaches maximum LOS velocities. Conversely, both in the east of this area (e.g., point 6) and in the west of this area (e.g., point 10), they show relatively lower LOS velocities. Hence, these inhomogeneities of LOS velocities along with the direction of graben clearly demonstrate that subsidence behavior varies spatially. This shows that there might be deep basins within the graben, which are controlled by structural lines extending approximately perpendicular or obliquely to the graben.

By using the developed software, the periodic movements at the PS points have been successfully determined. Thanks to this analysis, the characteristics of the deformations at the PS points were examined and modeled in detail. It has been demonstrated that the developed method can be used successfully, especially in modeling dynamic deformations due to external forces. Periodic effects on deformations can be determined in regions where deformations occur due to external effects (groundwater level change, precipitation change, temperature change, etc.), and external forces causing these effects can be examined in detail from InSAR data with the developed method. Moreover, the velocity values estimated according to the linear model from the displacement values that contain large amplitude periodic effects may cause false interpretations. By removing this periodic effect from the time series, more accurate velocity values can be obtained, the results can be interpreted more accurately, and region-specific solutions can be realized. By using the developed method and software, it is possible to estimate generally time-dependent linear velocity values by eliminating periodic effects due to external forces from InSAR data. Thus, dynamic deformations due to external forces can be successfully monitored from InSAR data, thanks to the developed method and software.

Acknowledgements This study was supported by TUBITAK 119Y180 with project number The Scientific and Technological Research Council of Turkey and CUBAP M800 with project number The Scientific Technological Research Council of Sivas Cumhuriyet University. MATLAB software used in this study are licensed by Sivas Cumhuriyet University. StaMPS and SNAP software were used for the process of InSAR data. The authors are grateful to the European Space Agency (ESA) for providing Sentinel 1 data.

Author contributions All authors contributed to the study conception and design. Material preparation data collection performed by YG, SG, and AD. Analysis was performed by KOH, FP, HE, and HD. The first draft of the manuscript was written by İT, CO, YG, and KOH all authors commented on previous versions of the manuscript. All authors read and approved the final manuscript**.**

Funding This study was supported by TUBITAK 119Y180 with project number The Scientific and Technological Research Council of Turkey and CUBAP M800 with project number The Scientific Technological Research Council of Sivas Cumhuriyet University.

Declarations

Conflict of interest The authors declare that they have no known competing financial interests or personal relationships that could have appeared to influence the work reported in this paper.

References

Allen CR (1974) Geological criteria for evaluating seismicity. Geol Soc Am Bull 86:1041–1057

Arikan M, Hooper A, Hanssen R (2009) Radar time series analysis over West Anatolia. Fringe 2009 Workshop; Frascati. 30 November–4 December (ESA SP-677, March 2010)

Arpat E, Bingöl E (1969) The rift system of the western Turkey; thoughts on its development. Bull Miner Res Explor Inst Turk 73(9)

Abdikan S, Arikan M, Şanli FB, Çakir Z, Kemaldere H (2013) Zonguldak Maden Alanlarında Meydana Gelen Yer Yüzeyi Hareketlerinin InSAR Zaman Serileri ile Belirlenmesi (Subsidence Monitoring in Zonguldak Coal Mining Area with SAR Interferometry). Harita Dergisi 149:1–6

Aktug B, Nocquet JM, Cingöz A, Parsons B, Erkan Y, England P, Lenk O, Gürdal MA, Kilicoglu A, Akdeniz H, Tekgül A (2009) Deformation of western Turkey from a combination of permanent and campaign GPS data: limits to block-like behavior. J Geophys Res: Solid Earth 114(B10)

Aktuğ B, Parmaksız E, Kurt M, Lenk O, Kılıçoğlu A, Gürdal MA, Özdemir S (2013) Deformation of central anatolia: GPS implications. J Geodyn 67:78–96

Bao L, Xing X, Chen L, Yuan Z, Liu B, Xia Q, Peng W (2021) Time series deformation monitoring over large infrastructures around Dongting Lake using X-band PSI with a combined thermal expansion and seasonal model. J Sensors 2021:1–17

Bekaert DPS, Walters RJ, Wright TJ, Hooper AJ, Parker DJ (2015) Statistical comparison of InSAR tropospheric correction techniques. Remote Sens Environ 170:40–47

Blewitt G, Lavallée D (2002) Effect of annual signals on geodetic velocity. J Geophys Res Solid Earth 107(B7):ETG-9

Bozkurt E (2001) Neotectonics of Turkey—a synthesis. Geodin Acta 14:3–30

Bozkurt E, Sözbilir H (2004) Tectonic evolution of the Gediz Graben: field evidence for an episodic, two-stage extension in western Turkey. Geol Mag 141:63–79

Bui LK, Le PV, Dao PD, Long NQ, Pham HV, Tran HH, Xie L (2021) Recent land deformation detected by Sentinel-1A InSAR data (2016–2020) over Hanoi, Vietnam, and the relationship with groundwater level change. Gisci Remote Sens 58(2):161–179

Burgmann R, Ayhan ME, Fielding EJ, Wright TJ, McClusky S, Aktug B, Demir C, Lenk O, Turkezer A (2002) Deformation during the 12 November 1999 Duzce, Turkey Earthquake, from GPS and InSAR Data. Bull Seismol Soc Am 92(1):161–171

Cakir Z, Akoglu AM, Belabbes S, Ergintav S, Meghraoui M (2005) Creeping along the Ismetpasa section of the North Anatolian fault (Western Turkey): Rate and extent from InSAR. Earth Planet Sci Lett 238(1–2):225–234

Crosetto M, Monserrat O, Cuevas-González M, Devanthéry N, Crippa B (2016) Persistent scatterer interferometry: a review. ISPRS J Photogramm Remote Sens 115:78–89

Dalaison M, Jolivet R (2020) A Kalman filter time series analysis method for InSAR. J Geophys Res Solid Earth 125(7):e2019JB019150

Darvishi M, Destouni G, Aminjafari S, Jaramillo F (2021) Multi-sensor InSAR assessment of ground deformations around Lake Mead and its relation to water level changes. Remote Sens 13(3):406

Demirtaş R, Yavuz MA, Şahin B (2008) Manisa ili, Sarıgöl ilçesi İmar Planı Sınırları içerisinde geçen Gediz Çöküntüsüne ait fay zonunun Paleosismolojik ve Yüzey Faylanması Tehlike Zonu Açısından Değerlendirilmesi. Afet İşleri Genel Müdürlüğü Raporu. 17s (yayınlanmamış)

Dikmen B, Uzun M, Aras M, Özaltın AM, Kirmencioğlu B, Özçam B (2019) Gediz Havzası Kuraklık Yönetim Planı Cilt 1, T.C. Tarım Ve Orman Bakanlığı Su Yönetimi Genel Müdürlüğü Taşkın Ve Kuraklık Yönetimi Dairesi Başkanlığı, Ankara (in Turkish)

Duman TY, Çan T, Emre Ö, Kadirioğlu FT, Başarır Baştürk N et al (2018) Seismotectonic database of Turkey. Bull Earthq Eng 16(8):3277–3316

Emre Ö, Özalp S, Duman TY (2011) 1:250.000 Scale Active Fault Map Series of Turkey, İzmir (NJ 35-7) Quadrangle. Serial Number: 6. Ankara, Turkey: General Directorate of Mineral Research and Exploration

Emre Ö, Duman TY, Özalp S, Şaroğlu F, Olgun Ş et al (2018) Active fault database of Turkey. Bull Earthq Eng 16(8):3229–3275. https://doi.org/10.1007/s10518-016-0041-2

Eser Mühendislik Müsavirlik AŞ (2014) DSİ 02 Bölge Gediz Havzası Yeraltısuyu Planlması-Hidrojeolojik Etüt Yaptırılması Ara Raporu (Proje Sahibi: DSİ İzmir Bölge Müdürlüğü)

Ferretti A, Prati C, Rocca F (2001) Permanent scatterers in SAR interferometry. IEEE Trans on Geosci Remote Sens 39(1):8–20

Frigo M, Johnson SG (1998) FFTW: an adaptive software architecture for the FFT. In: Proceedings of the 1998 IEEE international conference on acoustics, speech and signal processing, ICASSP'98 (Cat. No. 98CH36181), vol 3. IEEE, pp 1381–1384

Fuhrmann T, Garthwaite MC (2019) Resolving three-dimensional surface motion with InSAR: constraints from multi-geometry data fusion. Remote Sens 11(3):241
Fujiwara S, Nishimura T, Murakami M, Nakagawa H, Tobita M, Rosen PA (2000) 2.5-D surface deformation of M6. 1 earthquake near Mt Iwate detected by SAR interferometry. Geophys Res Lett 27(14):2049–2052
Gens R, Van Genderen JL (1996) SAR interferometry: issues, techniques, applications. Int J Remote Sens 17:1803–1835
Gezgin C (2022) The influence of groundwater levels on land subsidence in Karaman (Turkey) using the PS-InSAR technique. Adv Space Res 70(11):3568–3581
Hakyemez HY, Erkal T, Göktaş F (1999) Late Quaternary evolution of the Gediz ve Büyük Menderes Grabens, western Anatolia, Turkey. Quat Sci Rev 18:549–554
Hanssen RF (2001) Radar interferometry data interpretation and error analysis. Kluwer Academic Publishers, The Netherlands
Hastaoglu KO, Poyraz F, Turk T, Yılmaz I, Kocbulut F, Demirel M, Balik Sanli F (2018) Investigation of the success of monitoring slow motion landslides using Persistent Scatterer Interferometry and GNSS methods. Surv Rev 50(363):475–486
Hooper A, Zebker H, Segall P, Kampes B (2004) A new method for measuring deformation on volcanoes and other natural terrains using InSAR persistent scatterers. Geophys Res Lett 31(23):5. https://doi.org/10.1029/2004GL021737
Hooper A, Segall P, Zebker H (2007) Persistent scatterer InSAR for crustal deformation analysis, with application to Volcán Alcedo, Galápagos. J Geophys Res 112:B07407. https://doi.org/10.1029/2006JB004763
Hu X, Lu Z, Wang T (2018) Characterization of hydrogeological properties in salt lake valley, Utah, using InSAR. J Geophys Res Earth Surf 123(6):1257–1271
Hu J, Ge Q, Liu J, Yang W, Du Z, He L (2021) Constructing adaptive deformation models for estimating DEM error in SBAS-InSAR based on hypothesis testing. Remote Sens 13(10):2006
Ilieva M, Polanin P, Borkowski A, Gruchlik P, Smolak K, Kowalski A, Rohm W (2019) Mining deformation life cycle in the light of InSAR and deformation models. Remote Sens 11(7):745
Imamoglu M, Kahraman F, Cakir Z, Sanli FB (2019) Ground deformation analysis of Bolvadin (W. Turkey) by means of multi-temporal InSAR techniques and Sentinel-1 data. Remote Sens 11(9):1069
Khoshlahjeh Azar M, Hamedpour A, Maghsoudi Y, Perissin D (2021) Analysis of the deformation behavior and sinkhole risk in Kerdabad, Iran using the PS-InSAR method. Remote Sens 13(14):2696
Koca MY, Sözbilir H, Uzel B (2011) Sarıgöl fay zonu boyunca meydana gelen deformasyonların nedenleri üzerine bir araştırma. Jeoloji Mühendisliği Dergisi 35(2):151–174
Koçyiğit A, Yusufoğlu H, Bozkurt E (1999) Evidence from the Gediz Graben for episodic two stage extension in western Turkey. J Geol Soc Lond 156:605–616
Kürçer A, Özdemir E, Olgun Ş, Özalp S, Çan T, Elmacı H (2021) Active tectonic and paleoseismological characteristics of the Dinar Fault, SW Anatolia. Turk Mediterr Geosci Rev 3:219–251
Le Pichon X, Chamot-Rooke C, Lallemant S, Noomen R, Veis G (1995) Geodetic determination of the kinematics of Central Greece with respect to Europe: implications for Eastern Mediterranean tectonics. J Geophys Res 100:12675–12690
Lei K, Ma F, Chen B, Luo Y, Cui W, Zhou Y, Sha T (2021) Three-dimensional surface deformation characteristics based on time series InSAR and GPS Technologies in Beijing, China. Remote Sens 13(19):3964
Li Z, Zhao R, Hu J, Wen L, Feng G, Zhang Z, Wang Q (2015) InSAR analysis of surface deformation over permafrost to estimate active layer thickness based on one-dimensional heat transfer model of soils. Sci Rep 5(1):1–9
McClusky S, Aktuğ B, Aygül H, Baassanian S, Barka A, Burchfiel C, Çakmak R, Ergintav S, Hamburger M, Kahle H, Kastens K, King R, Kotzev V, Mahmoud S, Nadariya M, Özener H, Prilepin M, Reilinger R, Seeger H, Tari E, Türkezer A, Veis G (1999) GPS Constraints on active tectonics in the eastern mediterranean region. UNAVCO Meeting, Boulder CO. April 7–9
Massonnet D, Feigl KL (1998) Radar interferometry and its application to changes in the earth's surface. Rev Geophys 36(4):441–500
Meisina C et al (2006) Ground deformation monitoring by using the permanent scatterers technique: the example of the Oltrepo Pavese (Lombardia, Italy). Eng Geol 88:240–259
Morishita Y, Hanssen RF (2015) Deformation parameter estimation in low coherence areas using a multisatellite InSAR approach. IEEE Trans Geosci Remote Sens 53(8):4275–4283
Munteanu C, Negrea C, Echim M, Mursula K (2016) Effect of data gaps: comparison of different spectral analysis methods. Ann Geophys 34(4):437–449

Oral MB, Reilinger RE, Toksöz MN, Kong RW, Barka AA, Kınık İ et al (1995) Global positioning system offers evidence of plate motions in eastern Mediterranean. EOS Trans 76:9
Ozawa T, Ueda H (2011) Advanced interferometric synthetic aperture radar (InSAR) time series analysis using interferograms of multiple-orbit tracks: a case study on Miyake-jima. J Geophys Res: Solid Earth 116(B12)
Özkaymak Ç, Sözbilir H, Uzel B, Akyüz HS (2011) Geological and paleoseismological evidence for late pleistocene-holocene activity on the Manisa fault zone. Western Anatolia. Turk J Earth Sci 20:449–474
Özkaymak Ç, Sözbilir H, Geçievi MO, Tiryakioğlu İ (2019) Late Holocene coseismic rupture and aseismic creep on the Bolvadin Fault, Afyon Akşehir Graben. Western Anatolia. Turk J Earth Sci 28:787–880
Özkaymak Ç (2015) Tectonic analysis of the Honaz Fault (western Anatolia) using geomorphic indices and the regional implications. Geodin Acta 27(2–3):110–129
Paton S (1992) Active normal faulting, drainage patterns and sedimentation in southwestern Turkey. J Geol Soc Lond 149:1031–1044
Pawluszek-Filipiak K, Borkowski A (2020) Integration of DInSAR and SBAS Techniques to determine mining-related deformations using sentinel-1 data: the case study of Rydułtowy mine in Poland. Remote Sens 12(2):242
Peyret M, Rolandone F, Dominguez S, Djamour Y, Meyer B (2008) Source model for the Mw 6.1, 31 March 2006, Chalan–Chulan Earthquake (Iran) from InSAR. Terra Nova 20(2):126–133
Poyraz F, Hastaoğlu KÖ (2020) Monitoring of tectonic movements of the Gediz Graben by the PSInSAR method and validation with GNSS results. Arab J Geosci 13(17):1–11
Poyraz F, Hastaoğlu KO, Koçbulut F, Gursoy O (2016) Gediz Grabeninin Doğu Kesimindeki Tektonik Hareketlerinin GPS ve PS-InSAR Yöntemleri Kullanılarak Belirlenmesi. TUBİTAK 113Y526 Nolu 3501 Proje Sonuç Raporu
Poyraz FA, Hastaoğlu KO, Kocbulut Fİ, Tiryakioğlu I, Tatar OR, Demirel ME, Duman HÜ, Aydın C, Ciğer AF, Gursoy O, Turk TA (2019) Determination of the block movements in the eastern section of the Gediz Graben (Turkey) from GNSS measurements. J Geodyn 123:38–48
Poyraz F, Yavuz G, Duymaz B (2020) Determination of deformations by using the PSI technique at a common dump site of three different open-pit marble mines in Turkey. Turkish J Earth Sci 29(6):1004–1016
Reilinger RE et al (2006) GPS constraints on continental deformation in the Africa Arabia–Eurasia continental collision zone and implications for the dynamics of plate interactions. J Geophys Res 111:B05411. https://doi.org/10.1029/2005JB004051
Rosen PA, Hensley S, Joughin IR, Li FK, Madsen SN, Rodriguez E, Goldstein RM (2000) Synthetic aperture radar interferometry. Proc IEEE 88(3):333–382
Serco Italia SPA (2020) StaMPS: presistent scatterer interferometry processing—Mexico City 2021 (version 1.1). Retrieved from RUS Lectures at https://rus-copernicus.eu/portal/the-ruslibrary/learn-by-yourself/
Seyitoğlu G, Scott BC (1996) The age of Alaşehir graben (west Turkey) and its tectonic implications. Geol J 31:1–11
Shahzad N, Ding X, Wu S, Liang H (2020) Ground deformation and its causes in Abbottabad city, Pakistan from Sentinel-1A data and MT-InSAR. Remote Sens 12(20):3442
Shi W, Chen G, Meng X, Jiang W, Chong Y, Zhang Y, Zhang M (2020) Spatial-temporal evolution of land subsidence and rebound over Xi'an in western China revealed by SBAS-InSAR analysis. Remote Sens 12(22):3756
Sousa JJ, Ruiz AM, Hanssen RF, Bastos L, Gil AJ, Galindo-Zaldívar J, de Galdeano CS (2010) PS-InSAR processing methodologies in the detection of field surface deformation—study of the Granada basin (Central Betic Cordilleras, southern Spain). J Geodyn 49(3–4):181–189
Wang C, Zhang Z, Zhang H, Wu Q, Zhang B, Tang Y (2017) Seasonal deformation features on Qinghai-Tibet railway observed using time-series InSAR technique with high-resolution TerraSAR-X images. Remote Sens Lett 8(1):1–10
Yang YJ, Hwang C, Hung WC, Fuhrmann T, Chen YA, Wei SH (2019) Surface deformation from Sentinel-1A InSAR: relation to seasonal groundwater extraction and rainfall in Central Taiwan. Remote Sens 11(23):2817
Yao C, Cong P, Wan J, Li T, Liu L, Wang C, Zhang R, Fu Y, Lin T, Xu C, Lin X (2020) Spatio-temporal reductions of the COVID-19 lockdown-induced noise anomalies in GNSS height time series over mainland China. Remote Sens Lett 11(12):1118–1126
Yen JY, Lu CH, Chang CP, Hooper A, Chang YH, Liang WT, Chang TY, Lin MS, Chen KS (2011) Investigating active deformation in the northern longitudinal valley and city of Hualien in eastern taiwan using persistent scatterer and small-baseline SAR interferometry. Terr Atmos Ocean Sci 22(3):291–304
Yu C, Li Z, Penna NT, Crippa P (2018a) Generic atmospheric correction model for interferometric synthetic aperture radar observations. J Geophys Res Solid Earth 123(10):9202–9222

Yu C, Li Z, Penna NT (2018b) Interferometric synthetic aperture radar atmospheric correction using a GPS-based iterative tropospheric decomposition model. Remote Sens Environ 204:109–121
Zheng M, Deng K, Fan H, Du S (2018) Monitoring and analysis of surface deformation in mining area based on InSAR and GRACE. Remote Sens 10(9):1392
Zhu K, Zhang X, Sun Q, Wang H, Hu J (2022) Characterizing spatiotemporal patterns of land deformation in the Santa Ana Basin, Los Angeles, from InSAR time series and independent component analysis. Remote Sens 14(11):2624